Conference Proceedings of the Society for Experimental Mechanics Series

Chad Walber
Patrick Walter
Steve Seidlitz *Editors*

Sensors and Instrumentation, Aircraft/Aerospace, Energy Harvesting & Dynamic Environments Testing, Volume 7

Proceedings of the 38th IMAC, A Conference and Exposition on Structural Dynamics 2020

Springer

Conference Proceedings of the Society for Experimental Mechanics Series

Series Editor

Kristin B. Zimmerman, Ph.D.
Society for Experimental Mechanics, Inc.,
Bethel, CT, USA

The Conference Proceedings of the Society for Experimental Mechanics Series presents early findings and case studies from a wide range of fundamental and applied work across the broad range of fields that comprise Experimental Mechanics. Series volumes follow the principle tracks or focus topics featured in each of the Society's two annual conferences: IMAC, A Conference and Exposition on Structural Dynamics, and the Society's Annual Conference & Exposition and will address critical areas of interest to researchers and design engineers working in all areas of Structural Dynamics, Solid Mechanics and Materials Research.

More information about this series at http://www.springer.com/series/8922

Chad Walber • Patrick Walter • Steve Seidlitz
Editors

Sensors and Instrumentation, Aircraft/Aerospace, Energy Harvesting & Dynamic Environments Testing, Volume 7

Proceedings of the 38th IMAC, A Conference and Exposition on Structural Dynamics 2020

Springer

Editors
Chad Walber
PCB Piezotronics, Inc.
Depew, NY, USA

Steve Seidlitz
Cummins-Power Systems
Minneapolis, MN, USA

Patrick Walter
Texas Christian University
Fort Worth, TX, USA

ISSN 2191-5644 ISSN 2191-5652 (electronic)
Conference Proceedings of the Society for Experimental Mechanics Series
ISBN 978-3-030-47712-7 ISBN 978-3-030-47713-4 (eBook)
https://doi.org/10.1007/978-3-030-47713-4

This Springer imprint is published by the registered company Springer Nature Switzerland AG.
The registered company address is: Gewerbestrasse 11, 6330 Cham, Switzerland

Preface

Sensors and Instrumentation, Aircraft/Aerospace, Energy Harvesting & Dynamic Environments Testing represent one of eight volumes of technical papers presented at the 38th IMAC, A Conference and Exposition on Structural Dynamics, organized by the Society for Experimental Mechanics, and held in Houston, Texas, February 10–13, 2020. The full proceedings also include volumes on *Nonlinear Structures and Systems*; *Dynamic Substructures*; *Model Validation and Uncertainty Quantification*; *Dynamic Substructures*; *Special Topics in Structural Dynamics & Experimental Techniques*; *Rotating Machinery, Optical Methods & Scanning LDV Methods*; and *Topics in Modal Analysis &Testing*.

Each collection presents early findings from experimental and computational investigations on an important area within sensors and instrumentation and other structural dynamics areas. Topics represent papers on calibration, smart sensors, practical issues improving energy harvesting measurements, shock calibration and shock environment synthesis, and applications for aircraft/aerospace structures.

The organizers would like to thank the authors, presenters, session organizers, and session chairs for their participation in this track.

Depew, NY, USA — Chad Walber
Fort Worth, TX, USA — Patrick Walter
Minneapolis, MN, USA — Steve Seidlitz

Contents

Chapter 1
Orion MPCV E-STA Nonlinear Dynamics Uncertainty Factors

Matt Griebel, Adam Johnson, Brent Erickson, Andrew Doan, Chris Flanigan, Jesse Wilson, Paul Bremner, Joel Sills, and Erica Bruno

Abstract NASA vibration testing of the European Service Module (ESM) Structural Test Article (E-STA) for the Orion Multi-Purpose Crew Vehicle (MPCV) program demonstrated significant nonlinear behaviors and response deviation from pre-test finite element analysis (FEA). A linear FEA correlation effort, previously performed in 2017, resulted in the creation of two finite element models (FEM) – one correlated to high-load level swept sine responses and one correlated to low-load level swept sine responses. Additional work was required to quantify the uncertainty introduced when applying these linear models to non-sinusoidal flight load cases. To do this, an additional nonlinear dynamics model was developed and correlated with sine sweep test responses for low load level and high load level load cases. Results showed that, when the appropriate linearized model was selected for each specific Coupled Loads Analysis (CLA) loading type (i.e. Liftoff, Transonic, etc . . .), the linearized models closely matched predicted nonlinear responses with modest error (uncertainty factor). Results of this investigation have established a physics-based nonlinear dynamics approach that uses empirical test data to establish the credibility assumption for usage of linear FEM(s) in CLA. It is anticipated that the methodology employed can be extended for usage in correlation and flight loads analysis of subsequent spacecraft with major joint nonlinearities.

Keywords Nonlinear Dynamics · Uncertainty · Orion MPCV · Coupled Loads Analysis (CLA)

1.1 Introduction

MPCV E-STA sine vibration testing was performed at various flight-like load levels. Significant nonlinear behaviors were observed as well as response deviation from pre-test FEA. These nonlinearities were observable as significant frequency and damping shifts between the low-load level test cases (20% flight level loads) and the high-load level test cases (100% flight level loads). Sample sine sweep frequency response function (FRF) results are shown in Fig. 1.3. In addition, evidence of joint slipping onset was apparent in the test data FRFs, exhibited as nonlinear inflections in the ramp up to resonance.

A previous investigation by Quartus and NESC identified and limited the primary nonlinearities to three major interface joints. A linear FEA correlation effort resulted in the creation of two linear FEMs intended for use in a CLA study. The purpose of this study was to inform the use of correlated linear FEM(s) in a comprehensive linear CLA of a truly nonlinear system. One linear FEM was correlated to high level E-STA load cases (HLL FEM) and the other was correlated to low level E-STA load cases (LLL FEM). These two linear FEMs effectively represented linearizations of the true E-STA response about two specific load levels. Figure 1.1 illustrates how these linearizations might not necessarily predict accurate responses of a nonlinear system at load levels about which they were not correlated. Because of this, a single nonlinear FEM was created to help quantify the error (or uncertainty) introduced from utilizing linearized models in a linear CLA. This nonlinear "truth" model was developed from the previously correlated linearized models and correlated to the same E-STA sine sweep test

M. Griebel (✉) · A. Johnson · B. Erickson · A. Doan · C. Flanigan · J. Wilson
Quartus Engineering Incorporated, San Diego, CA, USA
e-mail: matt.griebel@quartus.com

P. Bremner
AeroHydroPLUS, Del Mar, CA, USA

J. Sills
NASA Engineering and Safety Center (NESC), Houston, TX, USA

E. Bruno
Analytical Mechanics Associates, Inc., Hampton, VA, USA

C. Walber et al. (eds.), *Sensors and Instrumentation, Aircraft/Aerospace, Energy Harvesting & Dynamic Environments Testing, Volume 7*, Conference Proceedings of the Society for Experimental Mechanics Series, https://doi.org/10.1007/978-3-030-47713-4_1

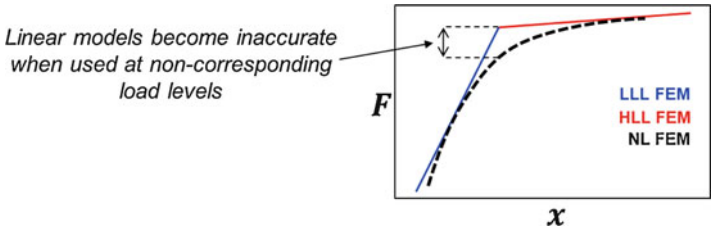

Fig. 1.1 Illustration of Linearization Uncertainty – A single nonlinear "truth" model can help quantify uncertainty introduced when the correlated HLL and LLL linear FEMs are used under a loading about which they were not correlated. (NOTE: Graphics generated in MATLAB 2018/2019 and MS Office 2016)

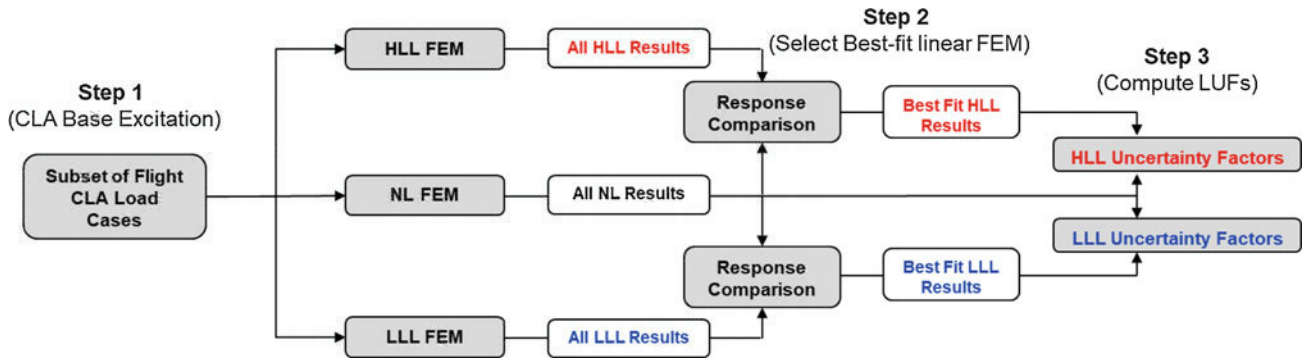

Fig. 1.2 CLA Study Outline – CLA response was compared between the linearized models and the nonlinear model resulting in the selection of a best-fit linearized model and corresponding LUF for each CLA loading type. (NOTE: Graphics generated in MATLAB 2018/2019 and MS Office 2016)

results. It included detailed representations of the nonlinear joints – primarily through the inclusion of Coulomb friction stick-slip conditions. The results of both the linear and nonlinear model correlation efforts are briefly summarized in this report; additional details of these correlation efforts can be found in their corresponding references [1, 2].

Figure 1.2 outlines the steps taken in a CLA study designed to assess the performance of the HLL and LLL FEM for a set of flight-like load cases. The study was performed using a subset of representative CLA load cases and compared the response of the HLL and LLL linearized models to the response of the nonlinear model. This subset of CLA load cases represented three distinct phases of flight:

- 5 Liftoff cases
- 6 Transonic cases
- 5 Max Acceleration cases

These CLA load cases (6 DOF acceleration time histories at the MPCV interface) were applied to all three models as a time domain base excitation (fixed base analysis). The HLL and LLL response time histories were then compared to the nonlinear response time histories and a best-fit linear FEM was selected to represent each CLA loading type. Linearization Uncertainty Factors (LUF) were then computed for each CLA loading type using the selected best-fit linear FEMs.

1.2 Analysis

A previous investigation performed by Quartus and NESC resulted in the creation of three correlated FEMs for use in a CLA study:

- LLL linearized model: Linear NASTRAN FEM correlated to E-STA response at 20% flight load levels
- HLL linearized model: Linear NASTRAN FEM correlated to E-STA response at 100% flight load levels
- Nonlinear "Truth" FEM: Single nonlinear Abaqus model representing E-STA response at all load levels

The results of both the linear and nonlinear model correlation efforts are briefly summarized in this report; additional details of these correlation efforts can be found in their corresponding references [1, 2]. The nonlinear Abaqus model is a combination of nonlinear Abaqus joints and a Hurty-Craig/Bampton (HCB) reduced model of the majority of the E-STA structure (reduction performed on NASTRAN model and HCB matrices converted to Abaqus format).

One of the primary metrics used in the model correlation process was comparing E-STA FEM and test FRFs based on the E-STA sine test drive inputs. The linearized model FRFs were directly computed in the frequency domain using NASTRAN (sol 111). Figure 1.3 shows a comparison between the E-STA measured sine test FRFs and the linearized model FRFs at the Launch Abort System (LAS) simulator (considered a representative response location for gauging primary mode responses). Results are shown for the high-load level sine sweep (100% flight loading shown in red) and low-load level sine sweep (20% flight loading shown in blue) load cases. In the case of the linear correlation, the high load level sine sweep was applied to the HLL FEM while the low load level sine sweep was applied to the LLL FEM. The two linearized models approximated the frequency and damping shift observed during the E-STA test, however effects of slipping joints observable in the test responses was not captured.

The nonlinear model FRFs were computed by post-processing time histories from a nonlinear direct transient simulation of the E-STA high level and low level sine sweeps. These simulations were performed using Abaqus implicit dynamics. Figure 1.4 shows the same comparison with E-STA test FRFs using only a single correlated nonlinear model. In this case, both the high-load level and the low-load level sine sweep transient inputs were applied to the same correlated nonlinear model in direct transient simulations in Abaqus. The use of this single nonlinear model showed improved correlation over the use of the two separate linearized models and captured the slipping onsets observed in the measured test FRFs. Because of this, the nonlinear model was considered a "truth" model and acted as a surrogate for the E-STA true nonlinear response.

A CLA response study was performed using the three correlated models discussed above. The purpose of this study was to determine a best-fit linearized model for each CLA loading type (i.e. Liftoff, Transonic, Max Acceleration) by comparing the linearized model responses to the response of the nonlinear "truth" model. Figures 1.5 and 1.6 show the ensemble of CLA response locations used in this study.

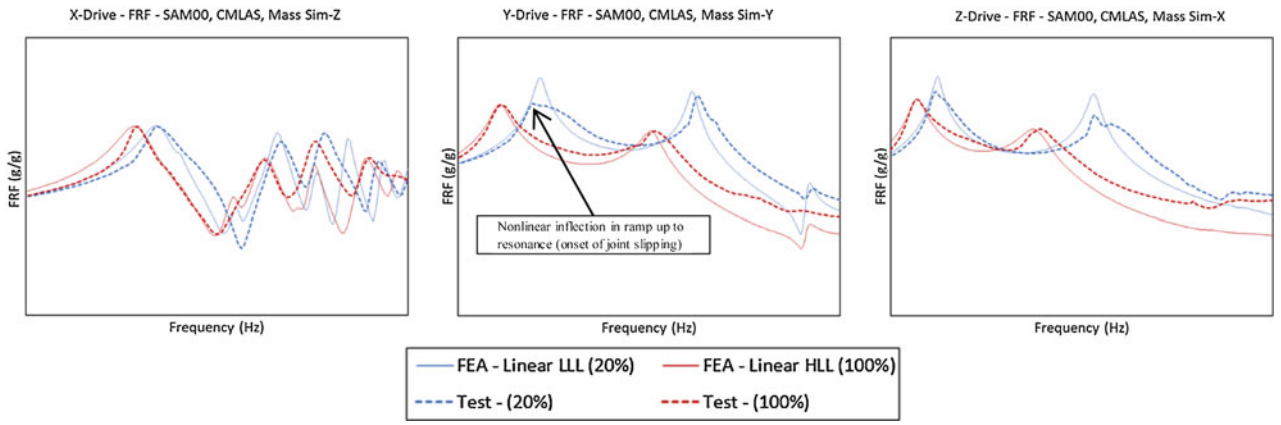

Fig. 1.3 Linear FEM Correlation Results (LAS Simulator FRF) – Two linear FEMs were able to approximate the frequency and damping shifts observed in test; however effects of joint slipping (evident in some test FRF peaks) could not be captured using two correlated linear FEMs. (NOTE: Graphics generated in MATLAB 2018/2019 and MS Office 2016)

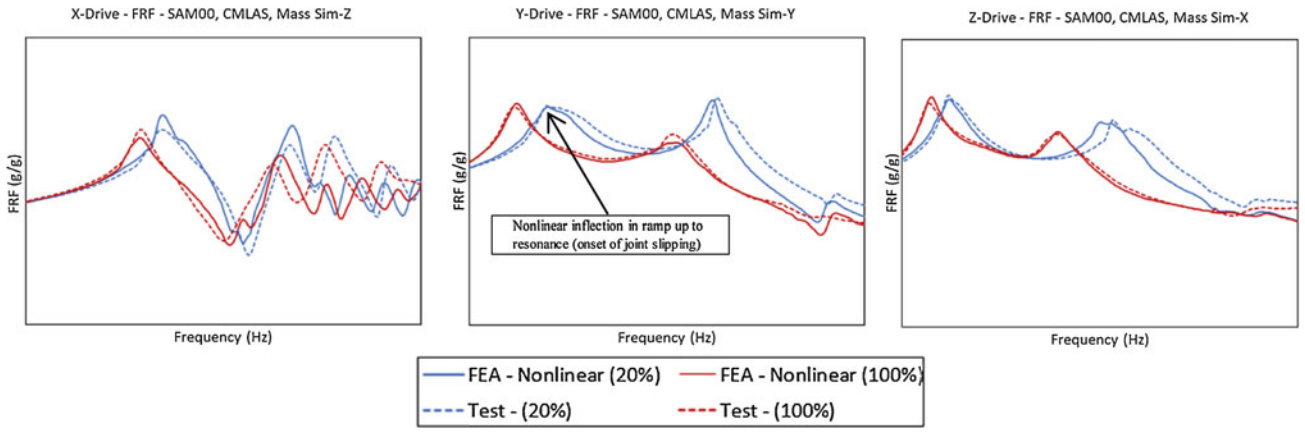

Fig. 1.4 Nonlinear FEM Correlation Results (LAS Simulator FRF) – A single correlated nonlinear FEM was able to capture frequency and damping shifts as well as effects of joint slipping observed in test. (NOTE: Graphics generated in MATLAB 2018/2019 and MS Office 2016)

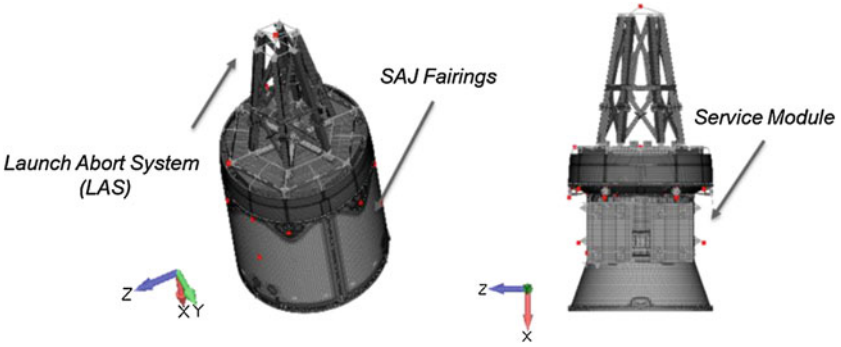

Fig. 1.5 Nodal Response Locations – CLA transient acceleration response was recovered in all translation DOFs at 27 nodal locations for the HLL, LLL, and nonlinear FEM. (NOTE: Graphics generated in Siemens Femap 11.3)

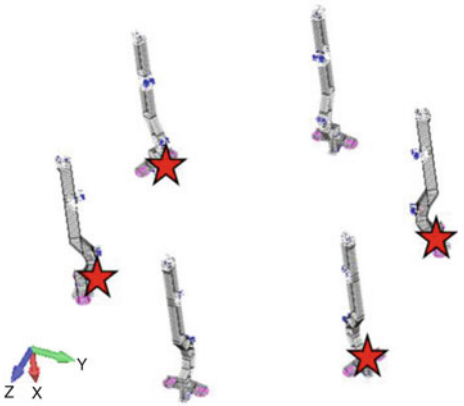

Fig. 1.6 Strain Response Locations – CLA transient strain response was recovered at 4 elemental locations for the HLL, LLL, and nonlinear FEM. (NOTE: Graphics generated in Siemens Femap 11.3)

Due to the large number of response outputs (i.e. locations, degrees of freedom [DOF], and load cases), Pearson Correlation Coefficients were used to compare the response of the HLL and LLL model to the nonlinear model for each output. A Pearson Correlation Coefficient is a time-integrated measure of the linear dependence of two variables (Eq. 1.1). When this is applied to two response time histories, it provides a high-level frequency and phase comparison. These are the most important metrics when determining which linearized model best represents the nonlinear response for any CLA loading type. It should be noted that the Pearson Correlation Coefficient is not sensitive to magnitude discrepancies between two time histories. These are accounted for in a subsequent computation of uncertainty factors after the best-fit linear models have been selected for each CLA loading type.

$$\rho\left(A, B\right) = \frac{1}{N-1} \sum_{i=1}^{N} \left(\frac{A_i - u_A}{\sigma_A} \right) \left(\frac{B_i - u_B}{\sigma_B} \right) \tag{1.1}$$

Pearson Correlation Coefficient – N: Sample Size, A&B: Random Variables, σ: sample standard deviation, μ: sample mean

Pearson correlation coefficients were calculated between each linearized model and the nonlinear model for all response locations over all load cases and grouped by their respective CLA loading types. Figure 1.7 shows histogram distributions of Pearson Correlation Coefficients representing the LLL and HLL acceleration response comparison with the nonlinear "truth" response. In addition, a representative sample transient response comparison is shown at a single node on the E-STA LAS simulator for each CLA loading type. For Liftoff and Transonic type load cases, a strong correlation was observed between the HLL linearized model and the nonlinear model. On the other hand, Max Acceleration load cases were a lower-level load case; therefore a strong correlation was observed between the LLL linearized model and the nonlinear model. The same trend was observed for strain response comparisons, but is not shown explicitly in this report. These trends informed the selection of the best-fit linearized models for each CLA loading type. The best-fit linearized model for Liftoff and Transonic CLA cases was the HLL FEM, while the best-fit linearized model for Max Acceleration CLA cases was the LLL FEM.

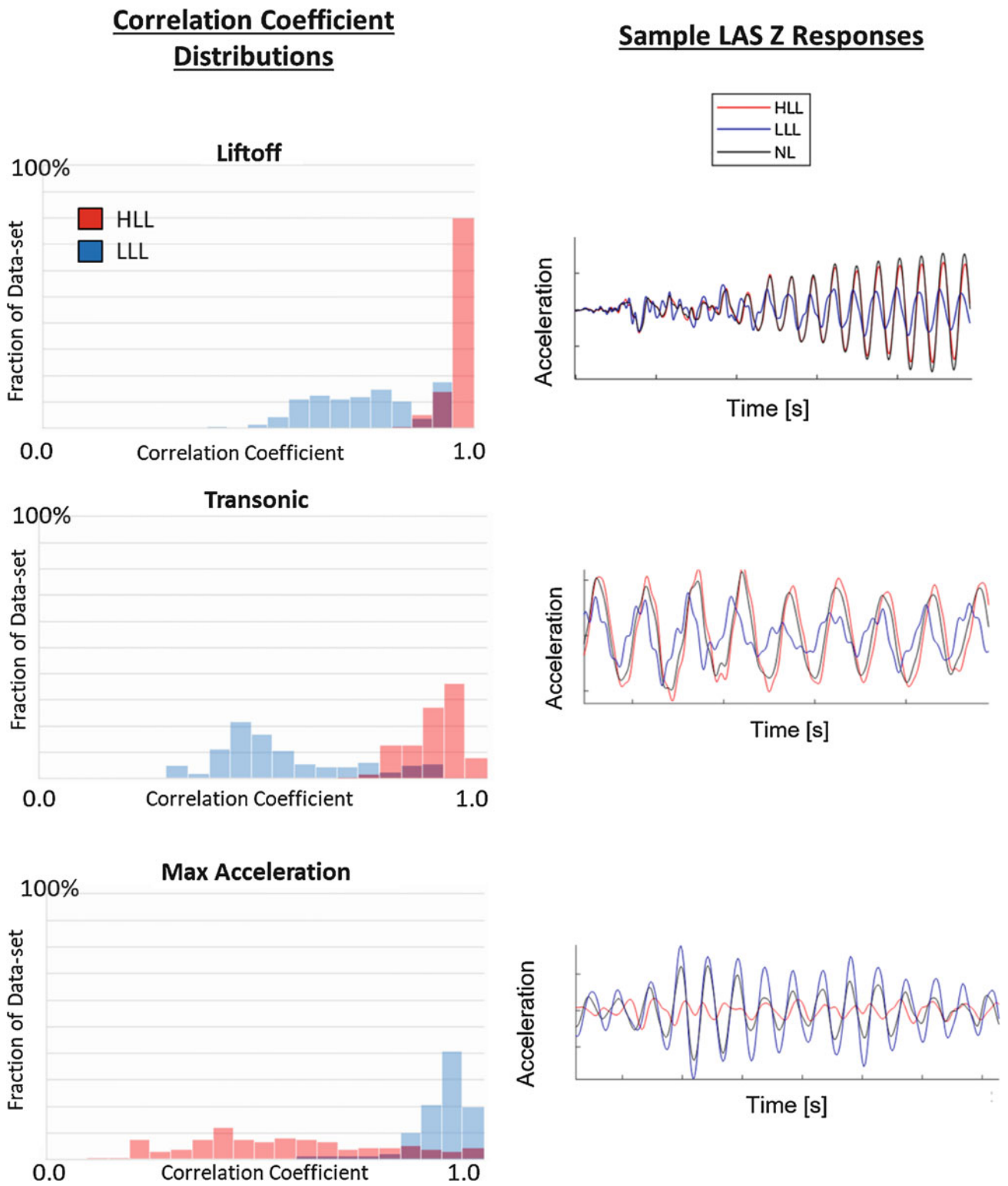

Fig. 1.7 Pearson Correlation Coefficients for Acceleration Response – Pearson Correlation Coefficients were computed between each linear model (LLL and HLL) and the nonlinear FEM and represented by histogram distributions. This was done to determine the best fit linear model for each CLA loading type. (NOTE: Graphics generated in MATLAB 2018/2019 and MS Office 2016)

Following the response comparison, Linearization Uncertainty Factors (LUF) were computed to represent the uncertainty that would be introduced using the selected best linear models in a comprehensive CLA. LUFs were computed for each CLA response location as a ratio of response magnitude between the nonlinear "truth" model and the selected best-fit linearized model (Eq. 1.2). Table 1.1 shows the selected response magnitude metrics for each CLA loading type. Because Liftoff and Max Acceleration load cases were non-stationary, peak-value was selected as the magnitude metric. Alternatively, since Transonic load cases were primarily random buffet loadings, root-mean-squared (RMS) was selected as the magnitude metric for these cases.

$$LUF_n = \frac{R_{NLin}}{R_{Lin}} \tag{1.2}$$

Linearization Uncertainty Factor – R_{Lin}: Linear response magnitude, R_{NLin}: Nonlinear response magnitude

By the definition in Eq. 1.2, the maximum LUF for any loading type was of primary interest as it represented instances in which the selected linear model was under-predicting the true nonlinear response. However, since this study was performed on only a subset of CLA load cases, a measure of statistical significance was desired to help characterize how well the computed max uncertainty factors can generalize a comprehensive CLA consisting of hundreds or thousands of load cases. Figure 1.8 shows Probability Density Functions (PDF) computed using LUFs from all response locations (including acceleration and strain).

Statistical significance is typically given as a probability level (β) and confidence level (γ) associated with a particular maximum value. In this case, it was observed that the LUF distributions were irregular (not Normal Gaussian distributions) rendering the standard Normal Tolerance methodology unusable within the current analysis parameters [3]. Investigation revealed that the irregularities observed were primarily due to the use of peak value as a magnitude metric for non-stationary load cases. For example, the Liftoff load cases consist of two distinct events – one in which the HLL model over-predicts the true nonlinear response, and another in which the HLL model under-predicts true nonlinear response. This results in the bi-modal probability distribution observed in the Fig. 1.8 Liftoff PDF.

A non-parametric, distribution-free methodology exists that does not assume any distribution of the sample [3]. The Distribution-Free Tolerance Limit (DFL) is defined as a value which exceeds all values for at least β fraction of a sample with a confidence γ defined by Eq. 1.3. The primary limitation of the DFL methodology is that it does not permit independent

Table 1.1 Determination of Response Magnitude Metric (R) for Each CLA Loading Type

	Type of Loading	Magnitude Metric	RSS DOFs
Liftoff	*Low Frequency*	*Peak Value*	*All*
Transonic	*Buffet + Thrust Osc.*	*RMS*	*YZ Lateral*
Max Acceleration	*Thrust Osc.*	*Peak Value*	*All*

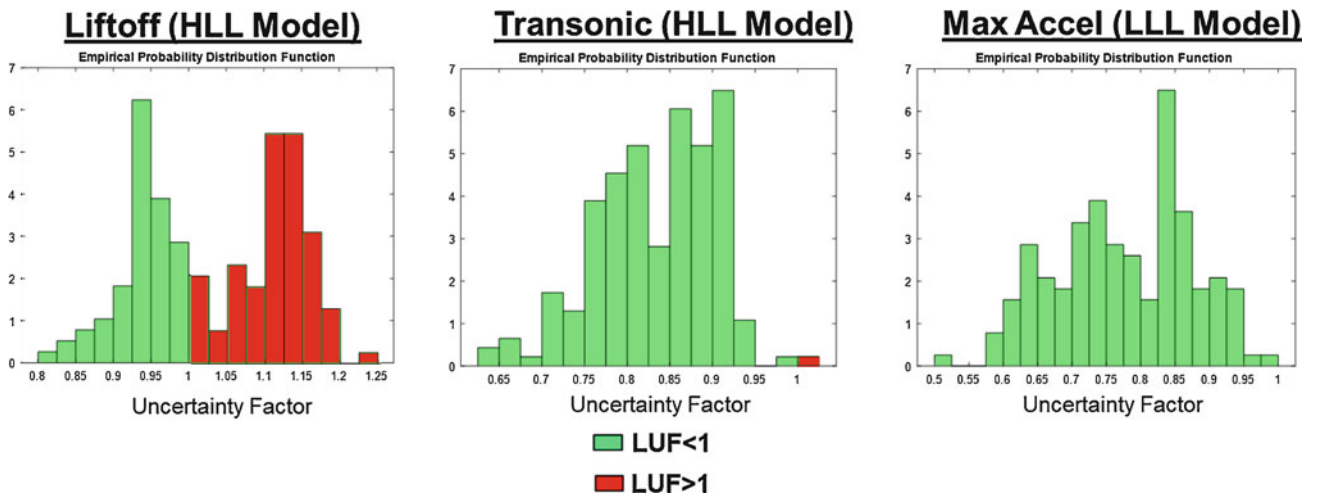

Fig. 1.8 Probability Density Functions of LUFs Computed Using Best-fit Linear Models – Probability distributions were determined to be irregular (not Normal Gaussian distributions). (NOTE: Graphics generated in MS Office 2016)

Table 1.2 Max Uncertainty Factors for Each CLA Loading Type

	Liftoff	Transonic	Max Acceleration
Max Uncertainty Factor	1.24	1.01	0.99
Selected Linear Model	High Load Level	High Load Level	Low Load Level
Probability	*98%*	*98%*	*98%*
Confidence	*96%*	*98%*	*96%*

selection of γ and β. Instead, $\beta < \beta_{max}$ is chosen to achieve desired confidence (where β_{max} is the fractional portion of the data enveloped by the max value). Since the LUF PDFs in Fig. 1.8 were extremely irregular (particularly the Liftoff distribution), further development of this methodology should be done to arrive at more familiar LUF distributions. This would allow for a better estimation of statistical significance.

$$\gamma = 1 - \beta^N \tag{1.3}$$

Confidence of Distribution-free Tolerance Limit (DFL) – Confidence associated with a DFL that envelopes β fraction of a sample (sample size = N)

Table 1.2 shows the max LUFs computed for each CLA loading type and an associated statistical probability and confidence (from the DFL methodology outlined above). Using the appropriate best-fit linear model for each loading type resulted in relatively modest maximum LUFs. It should be noted that inherent loads uncertainty as well as model uncertainty was not accounted for in this analysis. These additional sources of uncertainty would be combined with the LUFs to arrive at total CLA uncertainty.

1.3 Conclusion

NASA vibration testing of the Orion E-STA demonstrated significant nonlinear behaviors and response deviation from pre-test analysis. Because of this, two correlated linear FEMs were developed that acted as linearizations of E-STA response about low-load level (LLL FEM) and high-load level (HLL FEM). Additionally, a single correlated nonlinear "truth" model was developed to act as a surrogate for the E-STA true nonlinear response. A CLA response comparison study revealed that the linearized models can approximate the true nonlinear response and informed the selection of a best-fit linearized model. To account for the uncertainty introduced from performing a comprehensive linear CLA on a nonlinear system, Linearization Uncertainty Factors (LUF) were computed for each loading type. Using the best-fit linear FEM for each CLA loading type, it was found that modest LUFs could be applied to a comprehensive linear CLA.

Acknowledgements Special thanks to Joel Sills at NASA's Johnson Space Center (JSC) for his guidance and continued support of this assessment.

References

1. Doan, A., Erickson, B., Owen, T.: Orion MPCV E-STA Structural Dynamics Correlation for NASA NESC. El Segundo California, Spacecraft and Launch Vehicle (SCLV) Dynamic Environments Workshop (2018)
2. Griebel, M., Johnson, A., Erickson, B., Doan, A., Flanigan, C., Wilson, J., Bremner, P., Sills, J., Bruno, E.: Orion MPCV E-STA Nonlinear Correlation for NESC. El Segundo California, Spacecraft and Launch Vehicle (SCLV) Dynamic Environments Workshop (2019)
3. National Aeronautics and Space Administration: Computation of maximum expected environment. In: NASA Handbook 7005. Pasadena, CA: Jet Propulsion Laboratory, National Aeronautics and Space Administration (2017)

Chapter 2
The Vibration and Acoustic Effects of Prop Design and Unbalance on Small Unmanned Aircraft

William H. Semke, Djedje-Kossu Zahui, and Joseph Schwalb

Abstract The vibration and acoustic effects due to prop design, damage, and unbalance on a popular small unmanned aircraft systems (sUAS) is presented. The use of sUAS or drones is becoming ever more popular for hobbyists, as well as in commercial and military operations, and the influence of props on the vibration and acoustic environment are of interest. Many types of props are available for use on sUAS that promise extended run times, increased performance, and quieter operation. While many systems promise these results, few studies have been conducted to measure and evaluate their true performance. Therefore, this review provides data obtained by experimentally measuring the vibration levels onboard the host aircraft as well as the acoustic levels produced. The data is analyzed to gain further understanding of the vibration and acoustic properties and make predictions on prop performance. The fundamental frequencies of the aircraft are found along with the acoustic signature. These two outcomes are compared and studied to find the correlation between them. The analysis will utilize an airframes that is commonly used in the UAS community along with frequently used props that are balanced and unbalanced and with and without damage. The data is obtained from aircraft fully powered and airborne in a hovering or level flight configuration. This study provides sUAS operators the information required for choosing the most effective prop design to effectively reduce vibration and acoustic sound levels.

Keywords Unmanned aircraft · Remote sensing · Vibration · Sound levels · Acoustic testing

2.1 Introduction

Among the growing userbase of small Unmanned Air Systems (sUAS), the academic community takes a special interest in investigating their mechanical characteristics. Our focus exists in the mechanical characteristics and acoustic profile of the sUAS as a result to different styles of props and prop damage. There are multitudes of sellers carrying different types of propellers for the DJI Phantom 4 Pro, but we focus on select venders of propellers of two types: Standard and Low Noise. For both types of props, we examine the affect imbalance has on the vibration of the vehicle, as well as the change in acoustics introduced by the imbalance. The magnitude and spectral response of the system vibration and acoustic levels are presented.

Many types of props are available for use on sUAS that promise extended run times, increased performance, and quieter operation. A maritime engineering reference book examines different types of propellers and provides performance metrics and much of the analysis done by Carlson [1] assumes that the propeller is in an undamaged state. This tends to be a common assumption between similar works. The work presented here does not offer a fault-analysis of a damaged propeller, but the vibration characteristics and acoustic profile changes causal to a damaged propeller, in a controlled manner. The need to reduce or eliminate unwanted vibration in imaging systems is crucial in many applications of UAS. Researchers have carried out investigations into vibration isolation and active control for many years. Several studies [2–4] provide numerous resources into the basic principles. Given the limited range and payload capacity of these vehicles, vibration control is often carried out through passive means with vibration isolation and low noise and vibration blade design. Many researchers have carried out research into vibration isolation and active control over a long period of time and the fundamentals are explained in vibrations texts [5–7].

W. H. Semke (✉) · D.-K. Zahui
Department of Mechanical Engineering, University of North Dakota, Grand Forks, ND, USA
e-mail: william.semke@und.edu

J. Schwalb
Department of Aerospace Sciences, University of North Dakota, Grand Forks, ND, USA

C. Walber et al. (eds.), *Sensors and Instrumentation, Aircraft/Aerospace, Energy Harvesting & Dynamic Environments Testing, Volume 7*, Conference Proceedings of the Society for Experimental Mechanics Series, https://doi.org/10.1007/978-3-030-47713-4_2

Part of the inspiration for this paper stems from the want to "cut the cord" that we use to measure mechanical vibration of the vehicle. Specifically, we wanted to see if good correlation between mechanical vibration and acoustic profile exists. Should a strong correlation exist, it would allow vibration analysis with a microphone as opposed to an accelerometer attached to a cable. In other works, similar ideas have been explored for different reasons. Sas et al. [8] introduces experimental and numerical analysis of a multirotor chassis, with the goal of isolating areas of lesser vibrations. Their goal was to identify places of lesser vibrations so they could mount the more sensitive electronics in those areas. Kloet et al. [9] has a journal publication identifying the ambient noise of a multirotor UAS. They map the sound profile in two planes, adjacent to the propellers, and under the propellers. Dissent on experimentation analysis was done in the scope of both U. S. A. and E. U. regulators and their views of noise pollution in civil aviation. In an interesting turn, Iannace et al. [10] offers a fault diagnosis method for UAVs using artificial neural networks. In the process of building a model, they examine different imbalances by placing makeshift (tape) weights to introduce vibration. The model was trained to recognize the acoustics of the imbalanced propeller, to a success rate of 97% in the environment they tested in. Previous work by Semke, [11], offers analysis of different types of mounting mechanisms onboard a quadcopter and the vibration characteristics of the sensor mounting mechanisms of both multirotor and fixed wing aircrafts. The vibration environment onboard fixed-wing and quadrotor sUAS and provides sensor data to assist in passive and active vibration control methodologies [12].

2.2 Experimental Testing

In contrast to many related works today, the goal is to investigate and better understand what happens when there is a damage to the propeller. A critical question we draw attention to is how much damage influences the acceleration and acoustic levels and ultimately the flight performance of the sUAS.

Testing was performed on a DJI Phantom 4 Pro sUAS as shown in Fig. 2.1 Table 2.1 provides a key list of the aircraft specifications.

In this paper four sets of blades were tested in the laboratory. For each type of blade, vibration and acoustic measurements were simultaneously collected. Undamaged blades were tested first, then one centimeter from a single blade tip, on one side

Fig. 2.1 DJI Phantom 4 Pro UAS

Table 2.1 DJI Phantom 4 Pro Specifications

Weight	1388 g
Diagonal Size	350 mm
Max Speed	2 m/s
Max Flight Time	Approx. 30 minutes
Hover Range Accuracy	Vertical Accuracy: ±0.1 m (Vision Positioning), ±0.5 m (GPS Positioning) Horizontal Accuracy: ±0.3 m (Vision Positioning), ±1.5 m (GPS Positioning)

Fig. 2.2 Damaged propeller (left) and undamaged propeller (right) for the Standard 9450S and Low Noise 9455S

Table 2.2 Summary of Acceleration Testing of the DJI Phantom 4 Pro with Various Propeller Configurations

Blade Type	Amplitude: pk-pk (m/s^2)	Increase %	Standard Deviation (m/s^2)	Increase %
DJI OEM Standard	72		12	
DJI OEM Standard Damaged	127	76	21	75
BTG Standard	67		11	
BTG Standard Damaged	160	139	26	136
DJI OEM Low-Noise	70		11	
DJI OEM Low-Noise Damaged	93	33	17	55
Helistar Low-Noise	138		22	
Helistar Low-Noise Damaged	197	43	30	36

of the propeller, was removed to emulate damage. Figure 2.2 shows the damaged and undamaged props for the 4 types of props studied.

2.3 Vibration Testing

To measure vibrations, a PCB Model 333B30 single-axis accelerometer (10.5 $mV/m/s^2$) was attached to the base of the aircraft and the data was collected using a Data Physics Abacus 901 at a rate of 1536 Hz. The data was collected while the aircraft was in a hovering configuration approximately 1–2 meters above ground level. The peak-to-peak amplitude and the standard deviation for the recorded accelerations are shown in Table 2.2.

Table 2.2 illustrates several interesting findings observed from the accelerometer data. First, damage had a more dramatic impact on standard prop designs than it did with the low noise prop configurations. In the undamaged state, all props showed similar peak-to-peak and standard deviation amplitudes, except for the Helistar low noise prop. This prop design had significantly higher peak-to-peak and standard deviation amplitudes compared to all other undamaged prop formats. The highest increase in vibration amplitudes due to prop damage was observed in the BTG standard prop model. The lowest increased in vibration amplitudes due to prop damage was observed in the DJI OEM low noise prop model.

The Fast Fourier Transform (FFT) of each of the propeller configurations tests are shown in Figs. 2.3, 2.4, 2.5 and 2.6. The FFT plots show the frequency response of the aircraft for frequencies up to 600 Hz.

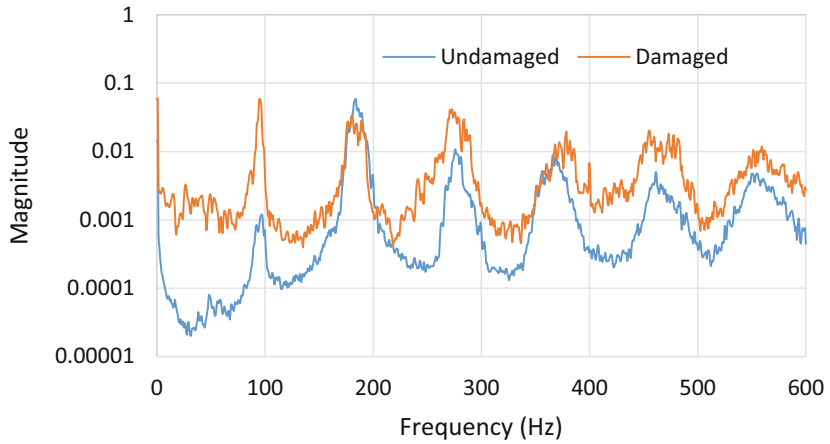

Fig. 2.3 DJI OEM 9450S Quick-Release Propellers FFT Comparison of Damaged and Undamaged Propellers

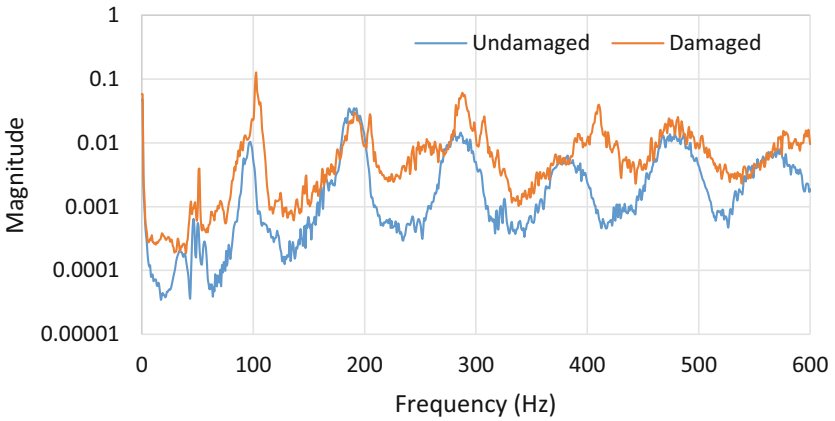

Fig. 2.4 BTG 9450S Quick-Release Propellers FFT Comparison of Damaged and Undamaged Propellers

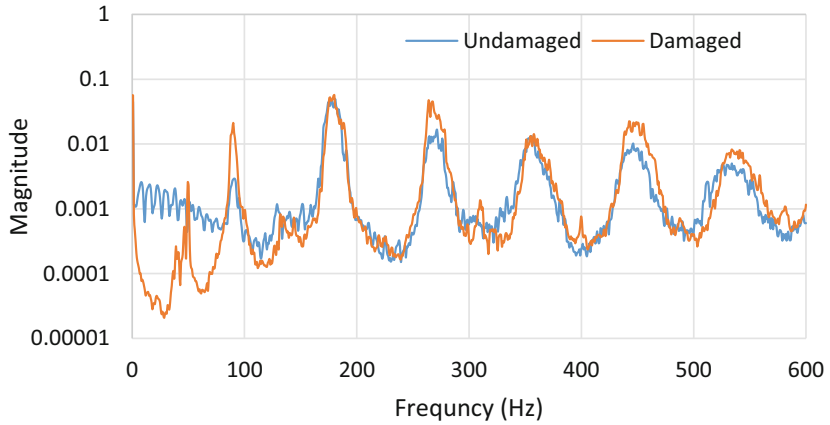

Fig. 2.5 DJI OEM 9455S Low-Noise Quick Release Propellers FFT Comparison of Damaged and Undamaged Propellers

The DJI OEM 9450S quick-release propellers FFT show a higher baseline and peak amplitudes across all frequencies with a damaged prop. The largest increase in amplitude occurred at frequencies under 150 Hz. The BTG 9450S quick-release propellers FFT shows a higher baseline and peak amplitudes across all frequencies when damaged as well. The highest increases occurred at frequencies below 150 Hz and between 200 and 450 Hz. The DJI OEM 9455S low-noise quick release propellers FFT did not show significant increase for most frequencies. Interestingly, there was a decrease in amplitude for most frequencies under 100 Hz along with an additional peak in the FFT plot around 50 Hz when the prop was damaged.

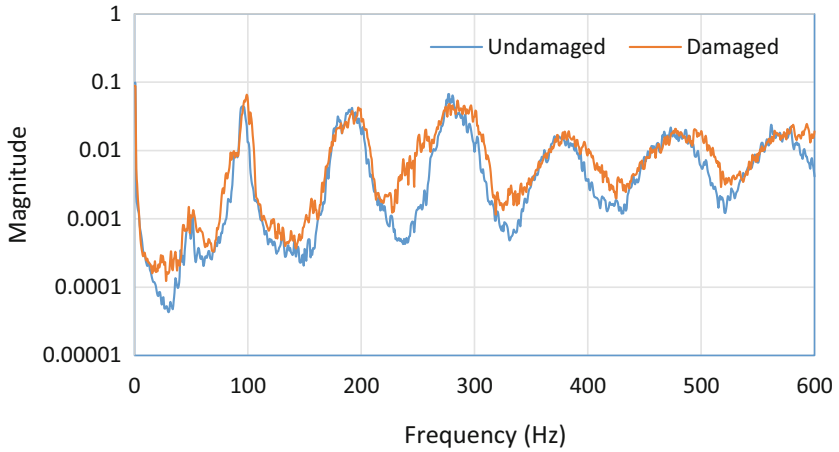

Fig. 2.6 Helistar 9455S Low-Noise Quick Release Propellers FFT Comparison of Damaged and Undamaged Propellers

The Helistar 9455S low-noise quick release propellers FFT only shows a slight increase across the frequencies studied with prop damage. This case showed the least impact of damage on the FFT results as the undamaged and damaged FFT plots closely mirrored each other.

2.4 Acoustic Testing

To measure noise, the ACO Pacific 4012 - 1/2 Inch directional microphone with a PS9200 2-channel power supply was used. The raw data was recorded using a TEAC LX-10 and later imported into MALAB® for analysis. Using a MATLAB® power spectrum analyzer object, a voltage spectrum was generated. The spectrum was then converted into Sound Pressure Lever (SPL) using the microphone sensitivity (50 mV/Pa). The results were converted into sound level[3] at each frequency in Pascal (Pa) and subsequently in dB with a $20\mu Pa$ reference pressure using Eq. (2.1).

$$L_i = 20\log_{10}\left(p_i/p_{ref}\right) \tag{2.1}$$

where L_i is the sound pressure in dB of the i^{th} frequency and p_i sound pressure in Pa. We also calculated the overall sound pressure level by combining the individual levels using Eq. (2.2).

$$L = 10\log_{10}\left(\sum\nolimits_i 10^{L_i/10}\right) \tag{2.2}$$

Figures 2.7a, 2.8a, 2.9a, and 2.10a depict the noise level spectrum and the overall SPL for the eight tests. The DJI and BTG standard blades show a 4 dB in noise level increase from the undamaged to the damaged props. The increase in noise level can also be related to the increased in vibration level for these blades as shown in Figs. 2.3, 2.4, 2.5, and 2.6 and Table 2.1. There was no significant change in noise level between the undamaged and damaged blades for both types of the low noise props. However, the vibration level was increased for these props. The overall sound pressure level results are summarized in Table 2.3. There were 4-dB increases in noise level for the DJI and BTG standard blades, while the low noise props by DJI and Helistar only saw 1 and 0 dB increases, respectively.

Further analysis of the data was carried out in the low frequency range (0–600 Hz) to better understand the correlation between the props radiated noise and vibration levels. Figures 2.7b, 2.8b, 2.9b, and 2.10b were thus generated. These figures represent the spectrum plot in Pascal (Pa) zooming in frequencies from 0 to 600 Hz. It can be seen on these sound pressure figures the frequency peaks correspond to the same frequencies as the vibration response frequency peaks. However, the peaks do not relate to the increase in sound pressure level from the undamaged to the damaged blades that were measured. For example, in Fig. 2.9b, the acoustic level peaks from the undamaged blade is higher than that of the damaged blade even though the overall sound pressure level indicates that the damaged blades were louder. The Figs. 2.7b, 2.8b, 2.9b, and 2.10b

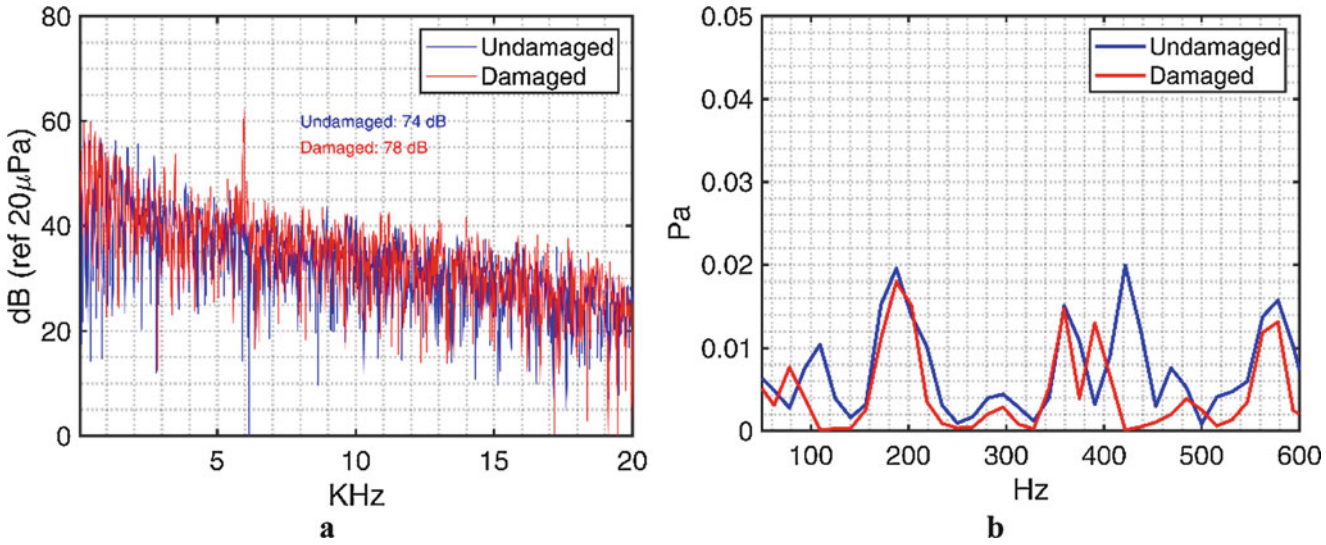

Fig. 2.7 DJI OEM 9450S Quick-Release Propeller Comparison of Damaged and Undamaged Propellers. (**a**) Noise Level Spectrum (**b**) Sound Pressure Spectrum

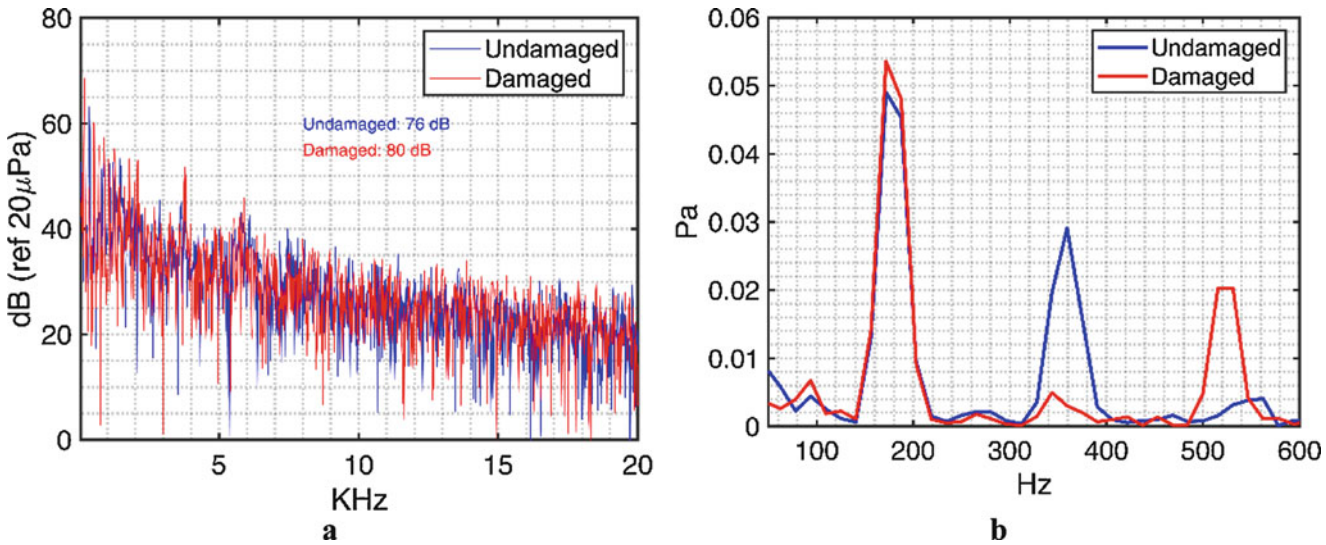

Fig. 2.8 BTG 9450S Quick-Release Propeller Comparison of Damaged and Undamaged Propellers. (**a**) Noise Level Spectrum (**b**) Sound Pressure Spectrum

Table 2.3 Summary of Sound Pressure Level of the DJI Phantom 4 Pro with Various Propeller Configurations

Blade Type	Sound Pressure Level (dB)	Increase (dB)
DJI OEM Standard	74	4
DJI OEM Standard Damaged	78	
BTG Standard	76	4
BTG Standard Damaged	80	
DJI OEM Low-Noise	74	1
DJI OEM Low-Noise Damaged	75	
Helistar Low-Noise	74	0
Helistar Low-Noise Damaged	74	

clearly show a correlation in frequency peaks between vibration and noise measurements. However, no definite conclusion can be drawn for the amplitude correlation between those two types of measurements.

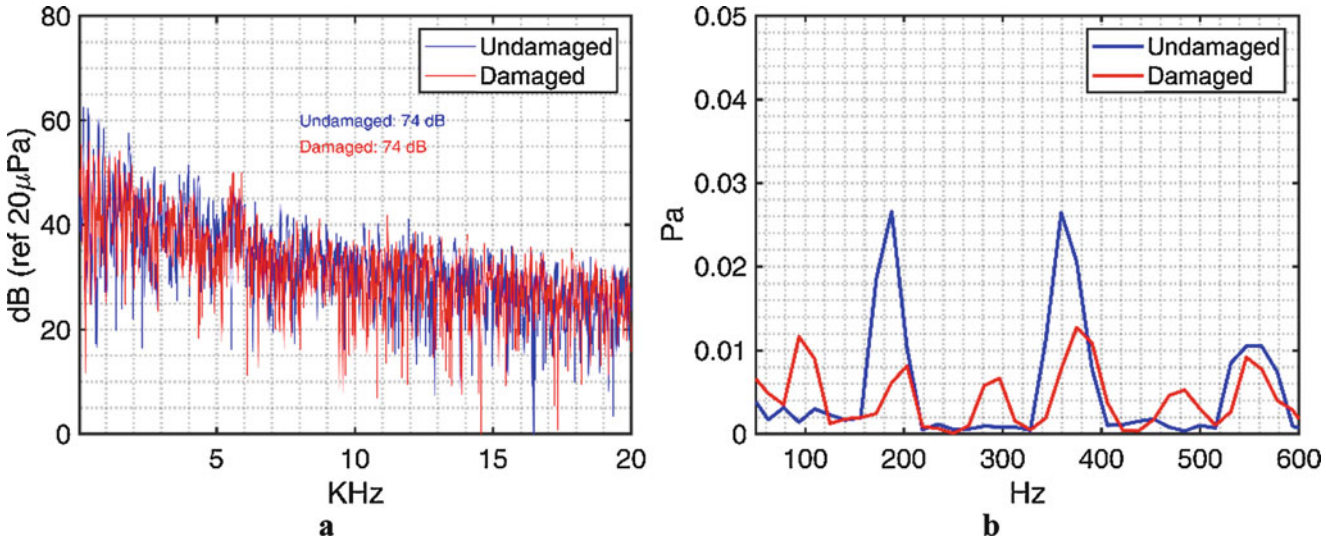

Fig. 2.9 DJI OEM 9455S Low Noise Quick-Release Propeller Comparison of Damaged and Undamaged Propellers (**a**) Noise Level Spectrum (**b**) Sound Pressure Spectrum

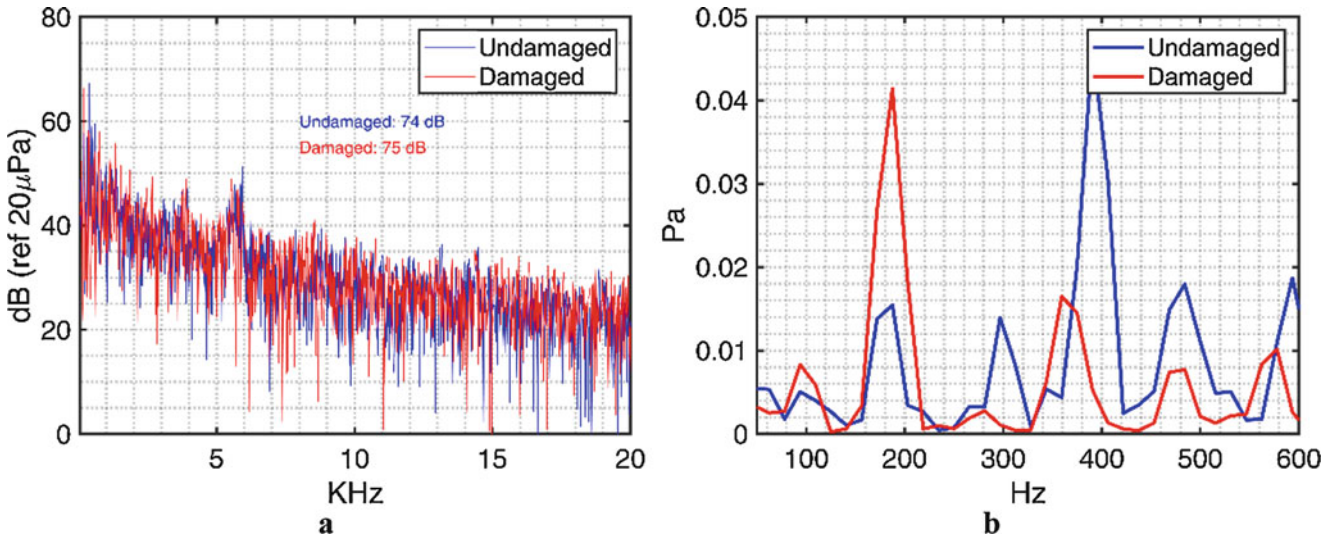

Fig. 2.10 Helistar 9455S Low Noise Quick-Release Propeller Comparison of Damaged and Undamaged Propellers (**a**) Noise Level Spectrum (**b**) Sound Pressure Spectrum

2.5 Conclusions

The extent of the damage to the props in this study did not greatly impact the flight performance of the aircraft. When the damage was introduced, the DJI Phantom 4 Pro did experience slight yawing when first taking off, but the internal flight controller quickly resolved this issue after becoming airborne and nominal flight performance was experienced. More significant, or damage to multiple props, may impart more dramatic and potentially catastrophic consequences resulting in an aircraft that is not airworthy. This greater damage was not studied in this analysis, only the relatively small damage that may result from small prop strikes or an unbalanced situation.

The observed vibration shows that the damage to the props increased both the peak-to-peak and standard deviation amplitudes for all configurations, but the damage had greater impact on the standard prop configurations. There was less impact in vibration due to the damage in the low noise configurations. The FFT amplitudes of the standard prop configurations showed a greater increase with damage. In general, the natural frequencies did not shift with damage except for the formation of an additional peak near 50 Hz in the damaged DJI OEM low noise prop.

The observed acoustics depicted an increase in sound pressure level and can be qualitatively related to the increase in vibration levels. It is therefore our belief that based on these preliminary findings a microphone or an array of microphones could be used to monitor the vibrations on a sUAV during mission. In the testing conducted only 2 microphones were used and the exact positioning of the aircraft was not maintained throughout all the testing. While the position was not exact, only small variations of less than 1 m were observed. Even though the direct amplitude correlation between increase noise level and increased vibration level could not be determined in the current data sets further testing could be done in the future to establish a clear relationship between the noise level of a sUAV with damaged props and the onboard vibration levels. The amplitude of the various acoustic results across the frequency bands investigated do not necessarily directly correlate with the amplitudes of the vibration modes experienced onboard the aircraft.

We believe further tests are needed to gain a better understanding of the behavior of sUAS props with a special emphasis on the low noise style. Greater prop damage magnitude and damage types will be investigated as well as a more detailed study on the correlation of vibration and acoustic responses. In this manner, we believe a non-invasive damage detection algorithm is possible using acoustic methods. This system would be part of robust and economical safety assessment procedures and protocols for preflight testing of remote autonomous sUAS systems that are planned for the future.

References

1. Carlton, J.S.: In: marine propellers and propulsion,. Butterworth-Heinemann,. In: Chapter 2 - Propulsion Systems, Cambridge, MA, United States (2019)
2. Thomas, R., Zahui, M.: Small unmanned aerial vehicle fuselage dynamic model using wings vibrations, Proceedings of the 22th international congress on sound and vibration. Florence, 12–16 July, 2015
3. Katalin, A.: Engineering Society International Conference 2017, MESIC" 11th international conference interdisciplinarity in engineering, INTER-ENG 2017, Tirgu-Mures, Romania, 5–6 Oct, 2017
4. Barron, R.F.: Industrial Noise Control and Acoustics, 1st edn. CRC Press (2002)
5. Crede, C.E.: Vibration and Shock Isolation. Wiley, New York (1951)
6. Rao, S.S.: Mechanical Vibrations. Prentice Hall, New Jersey (2004)
7. Meirovitch, L.: Fundamentals of Vibrations. McGraw-Hill, New York, NY, United States (2001)
8. Sas, P., et al.: Vibration Analysis of a UAV Multirotor Frame. KU Leuven - Department Werktuigkunde (2016)
9. Kloet, N., et al.: Acoustic signature measurement of small multi-rotor unmanned aircraft systems. Int. J. Micro Air Veh. 3–14 (2017). https://doi.org/10.1177/1756829316681868
10. Iannace, G., Ciaburro, G., Trematerra, A.: Fault diagnosis for UAV blades using artificial neural network. Robotics. **8**, 59 (2019)
11. Semke, W.: Vibration reduction for camera systems onboard small unmanned aircraft, Proceedings of the international modal analysis conference (IMAC) XXXVII: a conference and exposition on structural dynamics, 2019
12. Semke, W., Dunlevy, M.: A review of the vibration environment onboard small unmanned aircraft, Proceedings of the international modal analysis conference (IMAC) XXXVI: a conference and exposition on structural dynamics, 2018

Chapter 3
A Deformed Geometry Synthesis Technique for Determining Stacking and Cryogenically Induced Preloads for the Space Launch System

Joel Sills, Arya Majed, and Edwin Henkel

Abstract The Space Launch System (SLS) stacking and Core Stage (CS) fueling induce significant preloads that contribute to the liftoff pad separation "twang". To accurately capture this, an approach is required that can replicate the physics of all SLS physical stacking steps, CS cryogenic shrinkage, associated geometric nonlinearities, and the transient behavior and decay of the preloads with changing boundary conditions as the vehicle separates from the pad.

The Deformed Geometry Synthesis (DGS) approach presented here satisfies the above requirements. DGS determines induced preloads by modeling components in their deformed geometry states and then enforcing compatibility by closing the resulting "deadbands". DGS seamlessly integrates into the multibody modal synthesis framework and does not require the use of artificial external loads to enforce preloads or post-processing steps to remove their influence. Since DGS iterates to solve for the deformed state inclusive of geometric nonlinearities, running linearized parametrics to exercise different potential orientations of ball jointed struts that connect the CS to Boosters for cryo-shrinkage analyses is entirely avoided.

Relative to the transient behavior and decay of stacking and cryo-induced preloads with SLS liftoff pad separation, this is an area of considerable interest to the SLS program. To capture this in the most accurate way possible, DGS algorithms are designed to work with Henkel-Mar nonlinear pad separation algorithms which operate on the separating longitudinal and lateral degrees of freedom (DoFs) between the vehicle and the pad. As the separating DoFs release, in whatever manner as dictated by the interface geometries, interface loads and interface flexibilities as well as the external loading on the vehicle, the subject preloads generate a complex twang/decay time-trace as dictated by the physics of the problem.

This paper presents DGS numerical verification against the closed-form solution for Timoshenko's 3 ball-jointed strut preload problem. This problem is then extended by the authors to the geometric nonlinear case where DGS is compared to the Newton-Raphson solution of the nonlinear equations. Next, DGS is utilized to solve the SLS stacking and cryogenic shrinkage coupled loads analyses. Finally, Henkel-Mar pad separation simulations are executed that isolate the impact of the induced preloads' twang and decay characteristics.

Keywords Space launch system · Deformed geometry synthesis · Henkel-Mar pad separation · Geometric nonlinear

3.1 Introduction

A new approach for coupling deformed geometries and determining vehicle load indicators inclusive of prelaunch stacking and cryogenic induced preloads has been developed. This Deformed Geometry Synthesis (DGS) technique [1] is a specialized procedure in modal synthesis where components are coupled in their deformed geometry states by enforcing compatibility at the interfaces via a process of statically closing the resulting deadbands to lock-in the preloads. The procedure evokes a static version of the nonlinear deadband methodology first developed for the Space Shuttle Program (SSP). It has the advantage of being NASA verified and validated against test and utilized in the SSP nonlinear coupled loads analyses (CLAs) from 2005 until final flight in 2011.

To accurately capture the SLS stacking and cryo-induced preloads, DGS replicates the physics of all SLS physical stacking steps, Core Stage (CS) cryogenic shrinkage, associated geometric nonlinearities (e.g., aft strut rotations – a set of 3 ball

J. Sills (✉)
NASA Engineering and Safety Center (NESC), Houston, TX, USA
e-mail: joel.w.sills@nasa.gov

A. Majed · E. Henkel
Applied Structural Dynamics (ASD), Inc., Houston, TX, USA

C. Walber et al. (eds.), *Sensors and Instrumentation, Aircraft/Aerospace, Energy Harvesting & Dynamic Environments Testing, Volume 7*, Conference Proceedings of the Society for Experimental Mechanics Series, https://doi.org/10.1007/978-3-030-47713-4_3

jointed struts providing the aft connections for each booster to the CS), vehicle stabilizer system (VSS) coupling/preloads (see Sect. 3.4), mobile launcher (ML) extensible column/preloads (see Sect. 3.5), and the transient behavior and decay characteristics of the preloads with changing boundary conditions as the vehicle separates from the ML.

DGS seamlessly integrates into the SLS multibody modal synthesis framework and accurately simulates all stacking without the use of artificial external loads. The preloads are automatically reflected in the load indicator recoveries without any corrections or post-processing steps. All stages of stacking can be simulated including booster "toe-in" (for CS installation) and CS fueling/cryogenic shrinkage.

DGS starts with an initial deformed geometry state and solves for the final system deformed geometry state, inclusive of all preloads and geometric nonlinear effects. This process can proceed iteratively until desired convergence is achieved. With this, executing linearized parametrics to, for instance, exercise different potential aft strut orientations is avoided since geometric nonlinear effects are captured in the final deformed geometry. To reduce the number of iterations, the initial deformed geometry state can include 1G and thermal effects in order to quickly converge to the final state geometry. In practice, this is done and fully converged solutions are achieved in only two iteration steps.

The transient contribution (twang) and decay characteristics of the stacking and cryo-induced preloads is of considerable interest to the SLS program. To accurately capture this, DGS algorithms work together with Henkel-Mar nonlinear pad separation algorithms [2] which operate on the longitudinal and lateral separating DoFs at the ML to booster interface. As these separating DoFs release in the manner dictated by the interface geometries, interface flexibilities, interface loads, and external loads, the interaction of DGS and Henkel-Mar automatically generates the transient time-history, inclusive of the twang and decay characteristics, of the internal strain energy release.

A series of DGS verification problems involving a system of ball-jointed struts are provided in the next section to help make concepts crystal clear. The first set of these problems has a closed form solution provided by Timeshenko and Gere [3]. To verify DGS capability for capturing larger strut rotations, the Timshenko problem is extended to larger preloads. Here, the linear analytical solution no longer holds and DGS is compared with a Newton-Raphson nonlinear solution of the Timoshenko problem.

3.2 DGS Verification Problems

3.2.1 Verification Problem #1: Ball Jointed Strut Problem – Preloads (Linear Case)

Figure 3.1 depicts the ball-joint strut problem Timoshenko and Gere [3] utilized as the verification example. The vertical strut has an unstressed length of initial length (L) + change in length (ΔL). It is coupled into the diagonal struts resulting in compression of the vertical strut and associated extension/rotation of the inclined struts. The objective is to predict the strut loads, and the vertical displacement at the vertex.

The parameters used were: E = 10e6 psi, A = 1 in^2, L = 10 in, and ΔL = 0.125 in. Timoshenko and Gere [3] provided the following closed form solution for the strut loads as applicable for small displacements:

$$F_2 = \frac{2EA\,(\Delta L)\cos^3\beta}{L\left(1+2\cos^3\beta\right)}$$

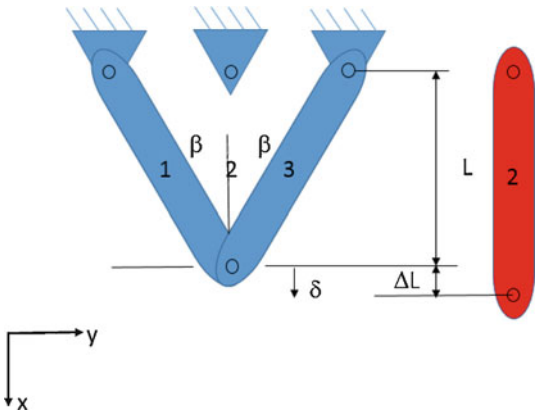

Fig. 3.1 Ball Jointed Strut Verification Problem (Timoshenko)

$$F_1 = F_3 = \frac{F_2}{2cos\beta}$$

$$\delta = \frac{F_2 L}{2EA\cos^3\beta}$$

From the above equations, it can be observed that the strut forces are a function of un-stressed strut lengths and un-deformed orientation which is characteristics of a linear problem. The comparisons to DGS for three orientations are provided in Tables 3.1, 3.2 and 3.3. Note in: this context, the Timoshenko analytical solution assumes small displacements. This problem is later extended to larger displacements, where Timoshenko analytical solution no longer holds.

3.2.2 *Verification Problem #2: Ball Jointed Strut Problem – Preloads (Nonlinear Case)*

For the nonlinear case, the ΔL is increased to 1.75 in. With this, the small displacement solution no longer holds and DGS iterations are required. The angle between the vertical and diagonal struts, $\boldsymbol{\beta}$, is initially set to 45° and is expected to decrease by a few degrees with the introduction of the preloaded vertical strut to the multibody system. The DGS solution is compared to the geometric nonlinear solution which utilizes Newton-Raphson. Results after 1 and 2 iterations are shown in Tables 3.4 and 3.5, respectively.

Table 3.1 DGS Verification Problem 1 – Preloads Case 1: $\boldsymbol{\beta} = 50°$

	Exact (analytical)	DGS (numerical)	Diff
F2	−43363.01	−43363.01	0
F1	33730.44	33730.44	0
F3	33730.44	33730.44	0
δ	8.1637e−2	8.1637e−2	0

Table 3.2 DGS Verification Problem 1 – Preloads Case 1: $\boldsymbol{\beta} = 5°$

	Exact (analytical)	DGS (numerical)	Diff
F2	−83015.02	−83015.02	0.
F1	41666.06	41666.06	0.
F3	41666.06	41666.06	0.
δ	4.1985e−2	4.1985e−2	0.

Table 3.3 DGS Verification Problem 1 – Preloads Case 1: $\boldsymbol{\beta} = 85°$

	Exact (analytical)	DGS (numerical)	Diff
F2	−165.29	−165.29	0.
F1	948.26	948.26	0.
F3	948.26	948.26	0.
δ	1.2483e−1	1.2483e−1	0.

Table 3.4 DGS Verification Problem 2 – Preloads Iteration Step 1

	Geometric Nonlinear*	DGS (numerical)	Diff
F2	−699700.	−675880.90	3.40%
F1	474220.	477919.97	−0.78%
F3	474220.	477919.97	−0.78%
δ	9.2787e−01	9.5584e−01	−3.01%
β	42.461°	42.388°	0.172%

Table 3.5 DGS Verification Problem 2 – Preloads Iteration Step 2

	Geometric Nonlinear*	DGS (numerical)	Diff
F2	−699700.	−700161.04	0.07%
F1	474220.	473987.38	0.05%
F3	474220.	473987.38	0.05%
δ	9.2787e−01	9.2731e−01	0.06%
β	42.461°	42.4625°	0.00%

3.3 Application to the SLS System

The SLS stacking procedures and cryogenic shrinkage due to the CS fueling induce significant preloads that contribute to the liftoff pad separation "twang". These preloads re-distribute and increase loads at the ML to boosters' separation interface and therefore impact the vehicle's pad separation dynamics. Figure 3.2 provides a depiction of the ML, boosters, CS, and Upper Stage (US).

Figure 3.3 provides a depiction of the aft struts connecting the CS to the boosters. When fueled, the CS shrinks both longitudinally and radially, rotating the aft struts in the longitudinal direction from the unfueled configuration and resulting in strut preloads.

The stacking steps start with the booster stacking, which simulates the ML vehicle support posts (VSPs) (Fig. 3.4) leveling, spacing and shimming under 1G deformed geometry. The boosters naturally "toe-in" as the ML "bows" under 1G. The shims ensure that the booster's forward attach interface (Fig. 3.5) to the CS is within the desired tolerance box to optimize the CS physical integration. The boosters are pulled apart for CS integration therefore inducing a "toe-in" preload and associated moment at the VSP interface which re-distributes the ML/booster interface loads. Given the unfueled CS CG off-set, the CS rotates away from the tower during stacking. This geometric nonlinear rotation step along with the delta rotation in the reverse direction to accommodate the integration of diagonal struts of a fixed length must be simulated in order to relieve this delta rotation which then preloads the diagonal struts. The next step in the stacking procedures involves simulating the upper and lower strut integrations which are adjusted to fill the space and therefore should have zero preloads at this stacking step.

Next the US components are integrated: Launch Vehicle Stage Adapter (LVSA), Interim Cryogenic Propulsion Stage (ICPS), MPCV Stage Adapter (MSA), and Multi-Purpose Crew Vehicle (MPCV) (see Fig. 3.6). Note that with this, the upper and lower aft struts are now taking load.

Fig. 3.2 SLS/ML Coupled System

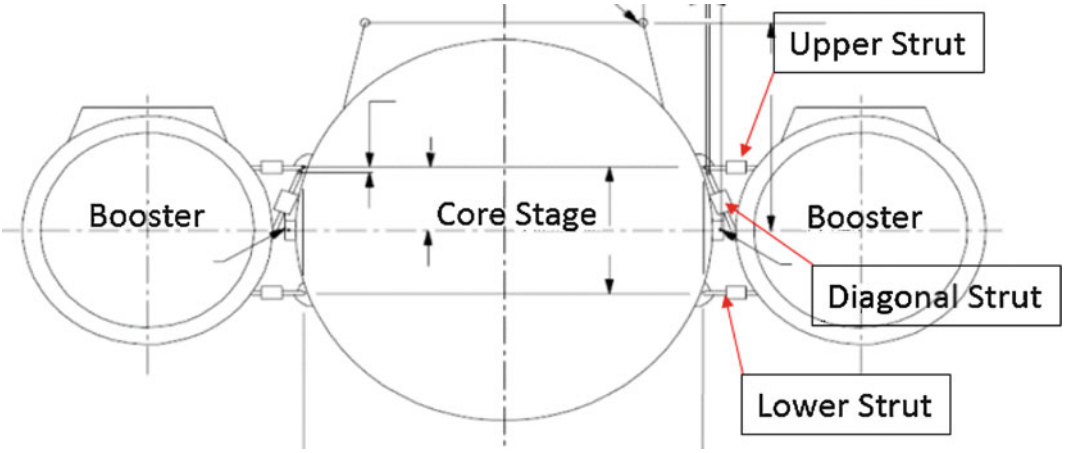

Fig. 3.3 CS/Boosters Aft Struts

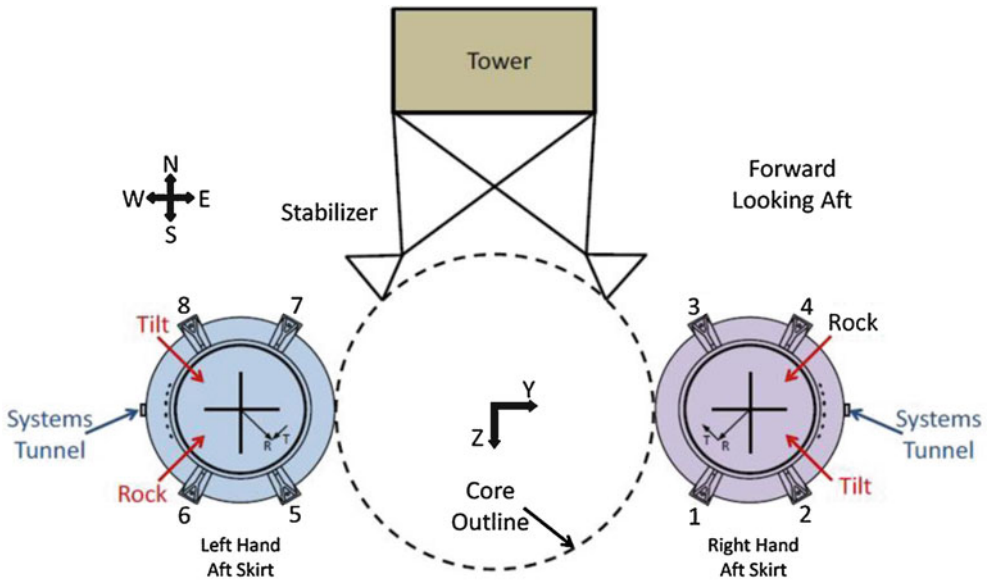

Fig. 3.4 Vehicle Support Posts (VSPs) Showing Inboard (odd) and Outboard (even) Numbering

The final step in the DGS simulations involves the CS cryogenic shrinkage which further adds to the vehicle preloads amplifying the pad separation twang.

3.4 DGS of Vehicle Stabilizer System (VSS) to the SLS

Figure 3.7 depicts the VSS which is designed to provide additional constraints against lateral displacements during the roll-out and prior to liftoff. The preloads at the VSS to CS interface are enforced via the DGS approach. At booster ignition, the VSS separates from the CS relieving the preloads at the subject interface.

The VSS includes radial and tangential hydraulic struts which are nonlinear. It is important for the VSS to be modeled in the coupled system as nonlinear given that at larger displacement amplitudes, the behavior of the nonlinear vs linearized VSS